Electronic Supplementary Information

Carved Nanoframes of Cobalt-Iron Bimetal Phosphide as a Bifunctional Electrocatalyst for Efficient Overall Water splitting

Yuebin Lian[a,b], Hao Sun[a,b], Xuebin Wang[a,b], Pengwei Qi[a,b], Qiaoqiao Mu[a,b], Yujie Chen[a,b], Jing Ye[c], Xiaohui Zhao[a,b], Zhao Deng[a,b*] and Yang Peng[a,b*]

a.Soochow Institute for Energy and Materials Innovations, College of Energy, Soochow University, Suzhou 215006, P. R. China.

b. Key Laboratory of Advanced Carbon Materials and Wearable Energy Technologies of Jiangsu Province, Soochow University, Suzhou 215006, P. R. China.

c. Analysis and Testing Center, Soochow University, Suzhou 215123, China.

Email: zdeng@suda.edu.cn; ypeng@suda.edu.cn.

Experimental details

Materials

Cobalt nitrate hexahydrate ($Co(NO_3)_2 \cdot 6H_2O$, 98%) was purchased from Sinopharm Chemical Reagent Co., Ltd.. Trisodium citrate dihydrate ($Na_3C_6H_5O_7 \cdot 2H_2O$, 99%), potassium hexacyanoferrate (III) ($K_3Fe(CN)_6$, 99%) and sodium hypophosphite monohydrate ($NaH_2PO_2 \cdot H_2O$, 98%), were purchased from Aladdin. Commercial Pt/C (Pt 20 wt.%) and RuO_2 purchased from Sigma-Aldrich. All the received without further purification and all the solvents used were of analytical grade.

Synthesis of Co-Fe PBA nanocubes.

Co-Fe PBA nanocubes were formed by a simple precipitation method. 0.6 mmol of cobalt nitrate hexahydrate and 0.9 mmol of trisodium citrate dihydrate were dissolved in 20 mL of deionized (DI) water to form solution A. 0.4 mmol of potassium hexacyanoferrate (III) was dissolved in 20 mL of DI water to form solution B. Then,

the solution B was added into the solution A under magnetic stirring. After continuous stirring for 1 min, the obtained mixed solution was aged at room temperature for 24 h. The precipitates were collected by centrifugation, followed by washing with DI water and ethanol, and dried at 70 °C overnight. The similar method is applied by changing cobalt nitrate hexahydrate to ferrous sulfate when preparing the Fe-Fe PBA and by changing hexacyanoferrate (III) to cobalt potassium cyanide when preparing Co-Co PBA.

Synthesis of Co-Fe PBA nanoframes

20 mg of the above prepared Co-Fe PBA nanocubes were dispersed into 40 mL of H_2O by ultrasonication for 10 min to obtain a homogeneous suspension. Then, 22.5 mg of urea were added into the above suspension with string for 20 min. After dissolving, the suspension was sealed into a 50 ml Teflon liner and then heated at 100 °C for 12 h in a stainless-steel autoclave.

Synthesis of Co-Fe-P nanoframes

The as-prepared Co-Fe PBA nanoframes were further annealed with NaH_2PO_2 at 300 °C for 2 h with a heating rate of 2 °C min^{-1} under a flow of N_2 atmosphere (100 sccm). In a typical process, 10 mg Co-Fe PBA nanoframes and 100 mg NaH_2PO_2 were placed in both sides of a quartz boat with NaH_2PO_2 at the upstream side of the furnace. The Co-Fe oxides were obtained with the same procedure but annealed in air.

Characterizations

The crystalline phase of the products was analyzed by powder XRD measurements with a Bruker D8 Advance X-ray diffractometer using Cu-Ka radiation and performed at a scanning rate of 0.1 s^{-1}. TGA (SDT 2960) was used to determine the optimum calcination temperature in order to obtain the best morphology and structures. Raman spectrum analysis (Horiba HR Evolution, with laser excitation at 633 nm sweep from 200 to 2500 cm^{-1}) was adopted to distinguish the characteristic vibrational modes of the synthesized materials, mainly for the D-band and G-band of the carbonized samples. The surface elemental states of the samples were analyzed with XPS, using an Escalab 250Xi X-ray photoelectron spectrometer with Mg Ka X-ray as the excitation source. The morphologies were examined by SEM using a Hitachi SU8010 scanning electron microanalyzer with an accelerating voltage of 10 kV. The microstructure of the samples was characterized by TEM measured at 200 kV with a FEI TECNAI G20 field-emission TEM. Elemental analysis of metal ions was determined by Inductively Coupled Plasma-Atomic Emission Spectrometry (ICP-AES) with an OPTIMA 8000 analyzer (PerkinElmer Inc.)

Electrochemical Measurements

4 mg Catalysts and 1 mg Ketjchen Black (KB) were dispersed in 800 μL of water, 200 μL of ethanol, and 50 μL of 5 wt% Nafion solution to form a homogeneous ink after

sonication for 30 min. For fabricating the working electrodes, 5 μL of the catalyst ink was loaded onto a glassy carbon (GC) electrode of 3 mm in diameter (loading amount was about 0.27 mg cm^{-2}) and then dried at room temperature. All the electrochemical measurements were performed in a standard three-electrode cell at room temperature using an electrochemical workstation (CHI660E). The graphite rod was used as the counter electrode, with the Ag/AgCl electrode (filled with saturated KCl) as the reference electrode. Prior to catalyst loading, the GC electrode was carefully polished with 1.0, 0.3 and 0.05 μm alumina powder in sequence, and cleaned by sonication in ethanol and deionized water. The electrolyte was 1.0 M KOH (pH=14) /0.5 M H$_2$SO$_4$ (pH=0.3)/1 M PBS (pH=7) bubbled with oxygen (or nitrogen) for 30 min prior to OER (or HER) measurements. All the potentials were converted to the potentials referring to the reversible hydrogen electrode (RHE), according to E (vs RHE) = E (vs Ag/AgCl) + 0.059 pH + 0.198. All of the potentials and voltages are obtained without iR correction unless otherwise noted.

Estimation of Effective Electrochemical Active Surface Area

The ECSA was obtained from the double layer capacitance (C$_{dl}$) of the catalyst surface. The C$_{dl}$ was determined by measuring cyclic voltammograms (CVs) with multiple scan rates within a non-faradaic potential region. The potential range was typically centered at the open circuit potential (OCP) with a potential window of 0.200 V. In this work, CVs were measured in a potential range of 0.225-0.425 V vs. RHE at different scan rates. The electrochemical double-layer capacitance was determined from the CV

curves measured in a potential range according to the following equation: $C_{dl} = I_c/v$, where C_{dl}, I_c, and v are the double-layer capacitance (mF cm^{-2}) of the electroactive materials, charging current (mA cm^{-2}), and scan rate (mV s^{-1}), respectively.

Calculation of the catalytically effective Co-Fe-P percentage

As shown in the Figure S11 the integral area of the oxidation peak is attributed to the irreversible oxidation of effective $Co_{0.6}Fe_{0.4}P$ sites in the catalyst. The whole oxidation is an 8-electron process:

$$Co_{0.6}Fe_{0.4}P + 11\ OH^- \rightarrow Co_{0.6}Fe_{0.4}OOH + PO_4^{3-} + 8\ e^- + 5\ H_2O$$
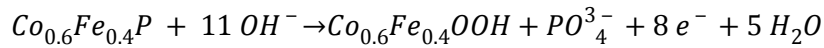
$$n_{effective} = \frac{Q}{nF} = \frac{0.0305\ C}{8 \times 96500\ C\ mol^{-1}} = 3.95 \times 10^{-8}\ mol$$

$$n_{total} = \frac{mAw}{M_w} = \frac{0.27\ mg\ cm^{-2} \times 0.07065\ cm^2 \times 84\%}{88.67\ g\ mol^{-1}} = 1.87 \times 10^{-7}\ mol$$

$$f = \frac{n_{effective}}{n_{total}} = 21.1\%$$

where Q is the total quantity of charge transfer derived from the oxidation of $Co_{0.6}Fe_{0.4}P$ and can be calculated by integrating the area of the oxidation peak. n is the electron transfer number of the oxidizing reaction, while F stands for the Faraday constant. m is the loading density of the catalyst and A is the working electrode area. w is the weight fraction of $Co_{0.6}Fe_{0.4}P$ in the catalyst which can be obtained from the TGA, Mw is the molecular weight of $Co_{0.6}Fe_{0.4}P$. The obtained f is the fraction of effective $Co_{0.6}Fe_{0.4}P$

sites and may be underestimated because of the absorbed oxygen on the surface and the incomplete oxidation of $Co_{0.6}Fe_{0.4}P$.

Calculation of the average turnover frequency (TOF) for HER and OER.

The TOF is a critical parameter to evaluate the electrocatalyst performance under a certain potential. The TOF of the catalyst can be calculated by quantifying the H_2/O_2 conversion per unit surface active site per unit time. Assuming a 100% faradic efficiency, then

$$TOF = \frac{IM_w}{nFAmw\,f} = \frac{I}{nFn_{effective}}$$

I is the current of the HER or OER at defined overpotential. Mw is the molecule weight of $Co_{0.6}Fe_{0.4}P$, n is the charge transfer number of the reaction, specifically n is 2 for H_2 and 4 for O_2, F is the Faraday constant, A is the area of working electrode, m is the loading density of the catalyst, and w is the mass fraction of $Co_{0.6}Fe_{0.4}P$ in the whole catalyst and f is the effective fraction of the $Co_{0.6}Fe_{0.4}P$. $n_{effective}$ is the effective molar amount of $Co_{0.6}Fe_{0.4}P$. The active site for OER is assumed to be $Co_{0.6}Fe_{0.4}OOH$ originated from the oxidation of the $Co_{0.6}Fe_{0.4}P$, and therefore the molar amount equals to $n_{effective}$.

Figure S12.a (HER) and Figure S12.b (OER) show the TOFs plotted for $Co_{0.6}Fe_{0.4}P$-1.125.

Calculation of the average grain size of the $Co_{0.6}Fe_{0.4}P$ nanoparticles in

nanoframes

The average grain size (D) of the CoFeP nanoparticles can be calculated using the Debye-Scherrer formula by identifying the intensity and width of a specific diffraction peak.
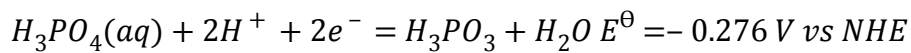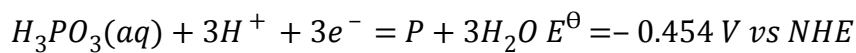
$$D = \frac{K\gamma}{B cos\theta}$$

Where K is the Scherrer constant and equals to 1 when B is the width of the diffraction peak, γ is the wavelength of X-ray, which is 0.154056 nm, B is the measured width of the chosen diffraction peak, which should be convert into rad, and θ is the bragg diffraction angle of the peak.

Possible phosphor-participated reactions in the HER process

The decreased content of P in the post-HER catalyst can be attributed to the oxidation of metal phosphides even at the applied HER potential. As indicated by the following reactions:

In acidic media (pH=0)

$H_3PO_3(aq) + 3H^+ + 3e^- = P + 3H_2O \ E^\Theta =- 0.454 \ V \ vs \ NHE$

$H_3PO_4(aq) + 2H^+ + 2e^- = H_3PO_3 + H_2O \ E^\Theta =- 0.276 \ V \ vs \ NHE$

In basic media(pH=14)

$HPO_3^{2-}(aq) + 2 \ H_2O + 2 \ e^- = P + 5OH^- \ E^\Theta =- 1.71 \ V \ vs \ NHE$

$PO_4^{3-}(aq) + 2H_2O + 2e^- = HPO_3^{2-}(aq) + 3OH^- \ E^\Theta =- 1.05 \ V \ vs \ NHE$
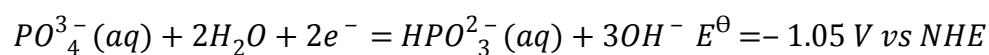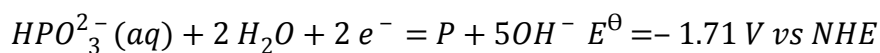
The HER overpotential is capable of converting phosphides into phosphates, which are soluble in the aqueous electrolyte.

Table S1. Summary of EDX and ICP results of Co-Fe bimetal phosphides.

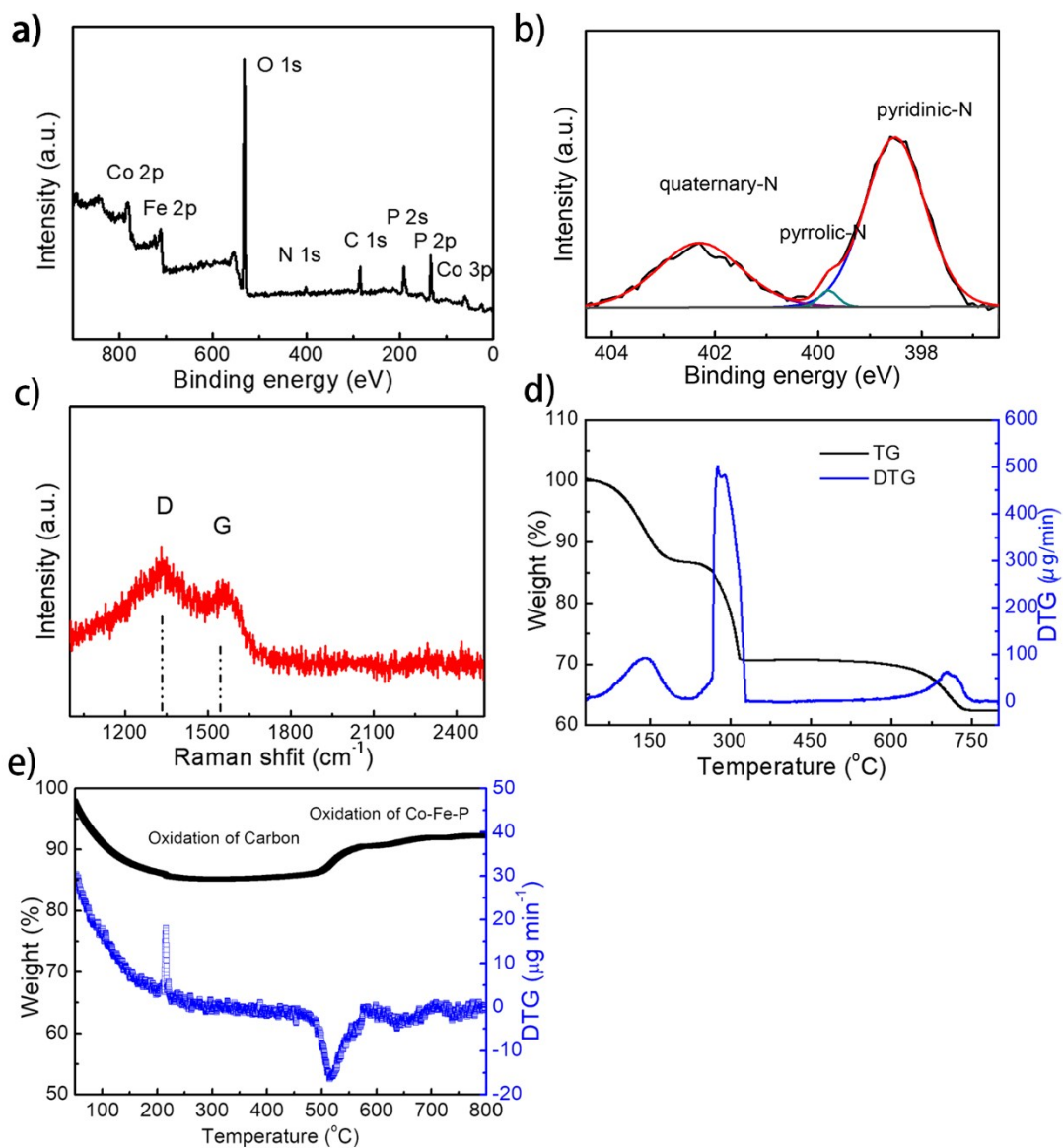| Sample	Co: Fe(EDX)	Co: Fe(ICP)	Theoretical value of Co:Fe by feeding ratio
Co0.6Fe0.4P-0	1.46	1.57	6:4
Co0.6Fe0.4P-1.125	1.48	1.54	6:4
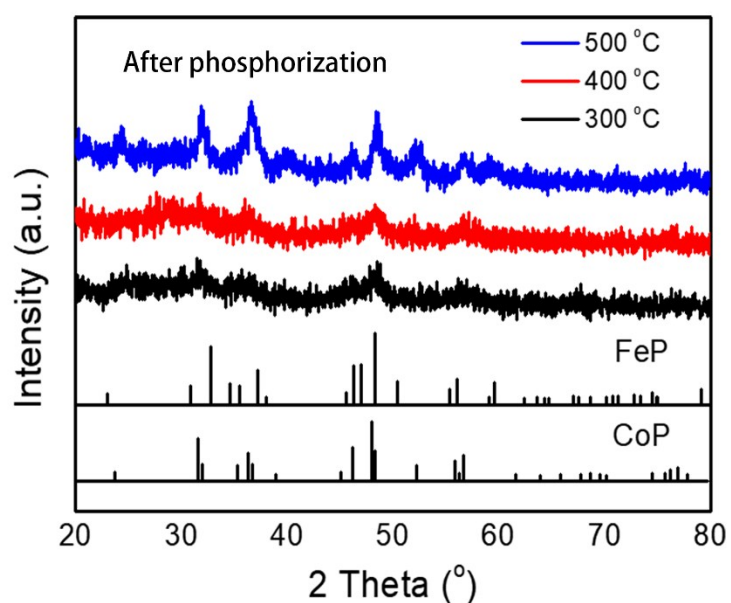
**Figure S1.** XRD patterns of $Co_{0.6}Fe_{0.4}P$-1.125 phosphorized at different temperature.
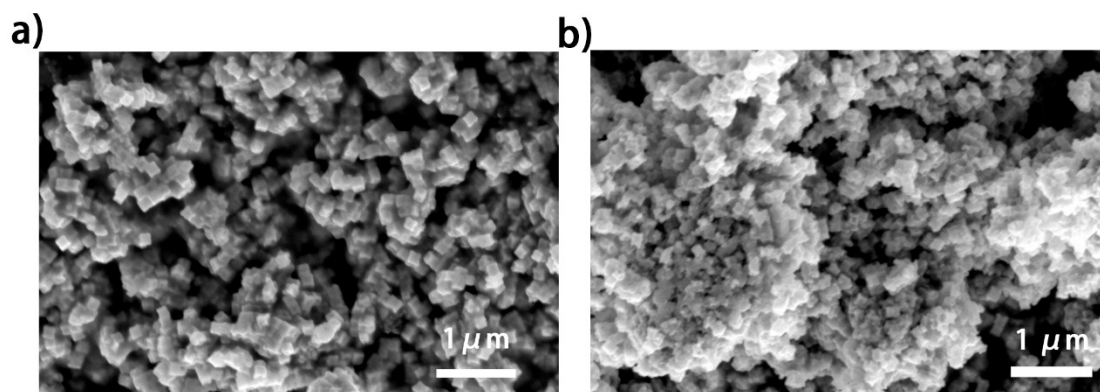
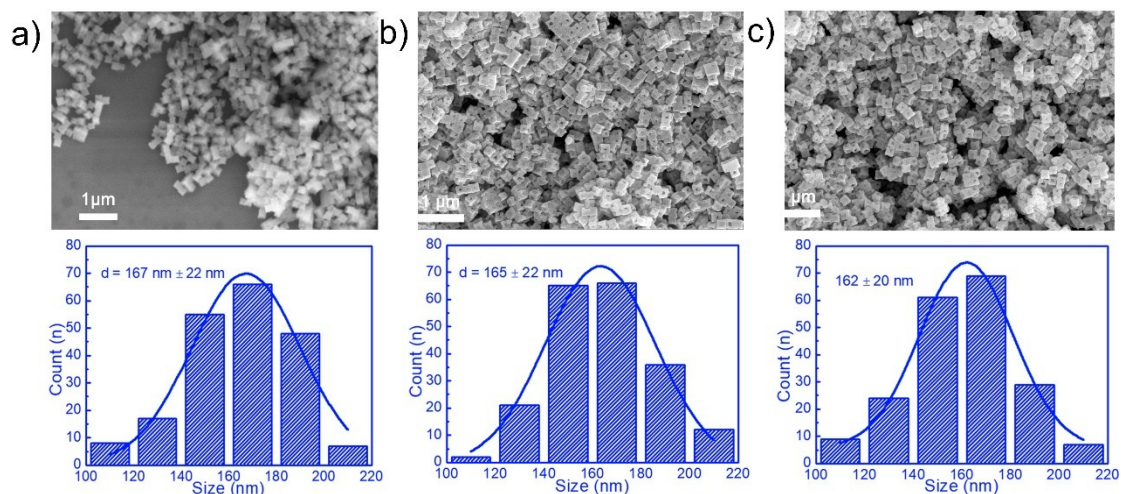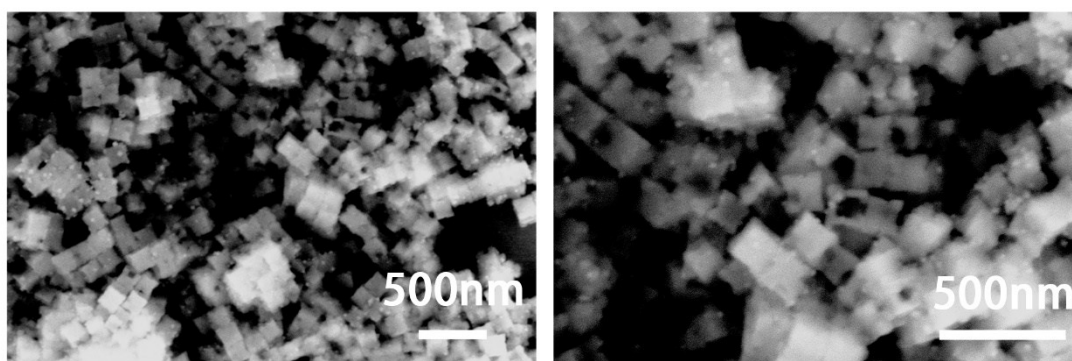**Figure S2.** SEM images of $Co_{0.6}Fe_{0.4}P$-1.125 phosphorized at a) 400 °C and b) 500 °C.

Figure S3. a) XPS survey spectrum of the $Co_{0.6}Fe_{0.4}P$-1.125 catalyst; b) High-resolution XPS N 1s spectra of the $Co_{0.6}Fe_{0.4}P$-1.125; c) Raman spectra of the $Co_{0.6}Fe_{0.4}P$-1.125 catalyst; d) Thermogravimetric analysis (TGA) of the $Co_{0.6}Fe_{0.4}$ PBA in air; e) Thermogravimetric analysis (TGA) of the $Co_{0.6}Fe_{0.4}P$-1.125 in air.
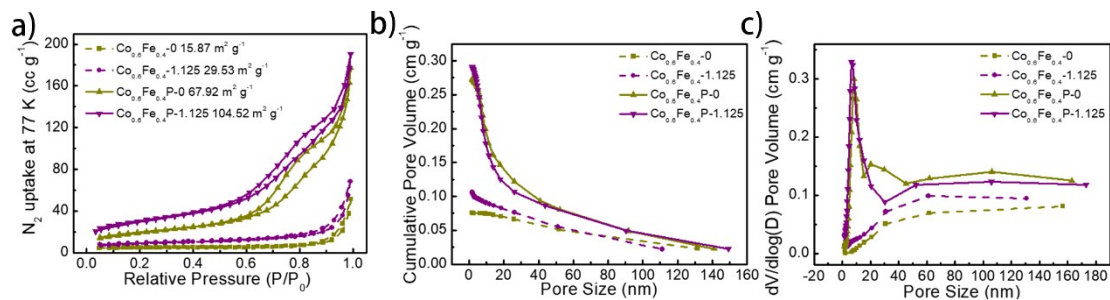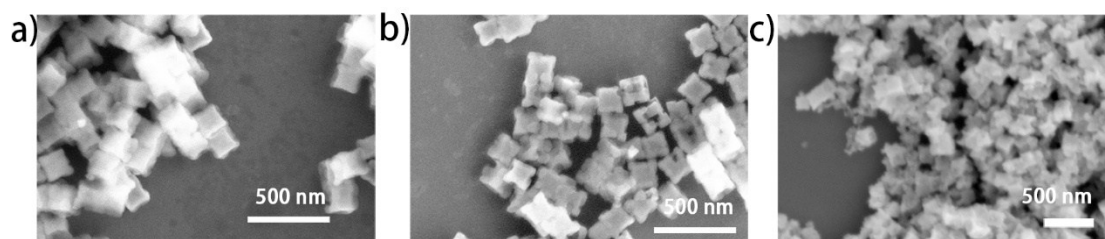
Figure S4. a) N_2 sorption isotherms of the catalysts at 77 K; the corresponding b) pore volume and c) pore size distribution.
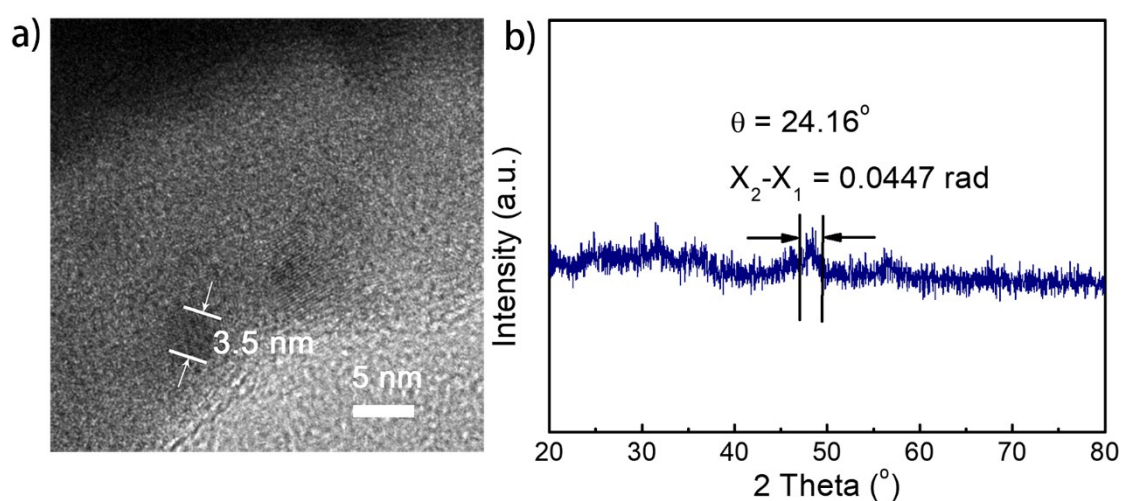

**Figure S5.** The SEM image and particle size distribution of a) $Co_{0.6}Fe_{0.4}$-0, b) $Co_{0.6}Fe_{0.4}$-1.125, and c) $Co_{0.6}Fe_{0.4}P$-1.125.


Figure S6. SEM images of $Co_{0.6}Fe_{0.4}$ PBA etched with ammonium.

Figure S7. a) SEM image of $Co_{0.6}Fe_{0.4}$-0.375 before phosphorization; b) SEM image of $Co_{0.6}Fe_{0.4}$-0.75 before phosphorization; c) SEM image of $Co_{0.6}Fe_{0.4}$-1.5 before phosphorization.

**Figure S8.** a) HRTEM of $Co_{0.6}Fe_{0.4}P$-1.125; b) XRD Debye-Scherrer calculations of the average particle size for $Co_{0.6}Fe_{0.4}P$-1.125.
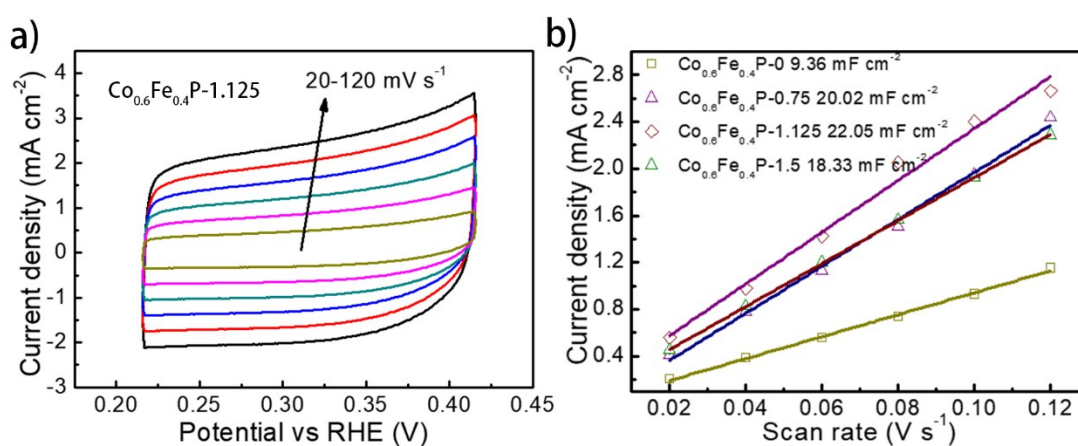
Figure S9. a) Cyclic voltammograms recorded at various scan rates in the non-Faradaic region in 0.5 M H_2SO_4 for the $Co_{0.6}Fe_{0.4}P$-1.125 catalysts; b) the current density as a function of scan rate for all $Co_{0.6}Fe_{0.4}P$ catalysts.
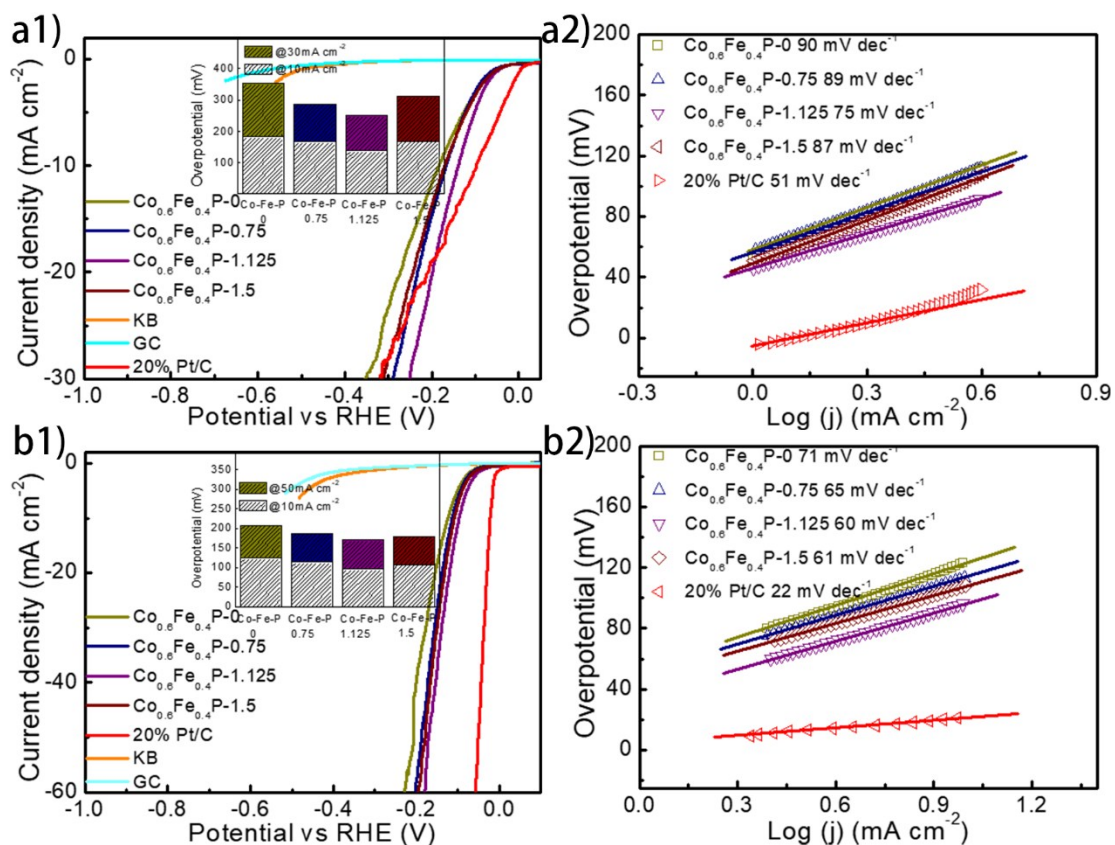
Figure S10. a1) LSV curves of various $Co_{0.6}Fe_{0.4}P$ and control samples for HER in 1.0 M PBS and a2) the corresponding Tafel plots of the $Co_{0.6}Fe_{0.4}P$ and Pt/C samples; b1) LSV curves of various $Co_{0.6}Fe_{0.4}P$ and control samples for HER in 0.5 M H_2SO_4 and b2) the corresponding Tafel plots of the $Co_{0.6}Fe_{0.4}P$ and Pt/C samples.
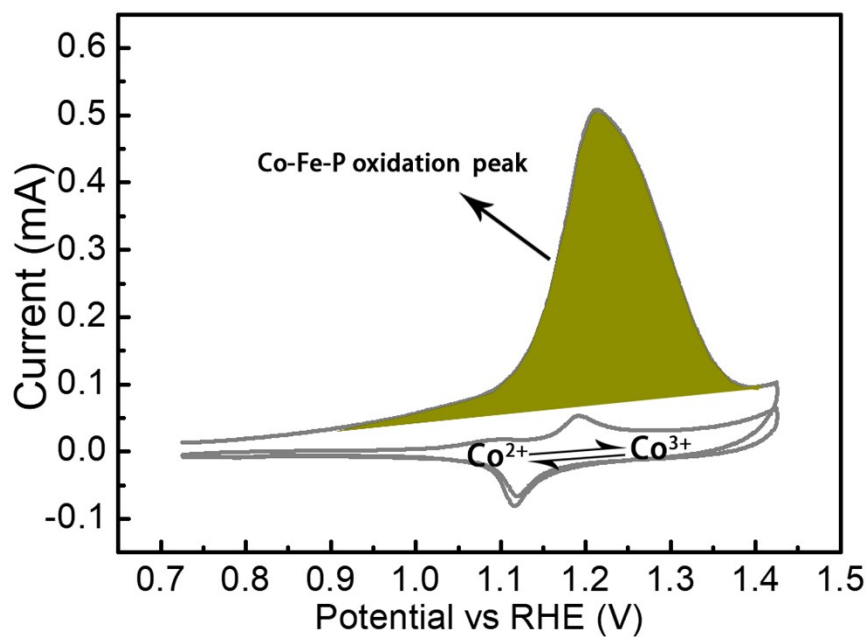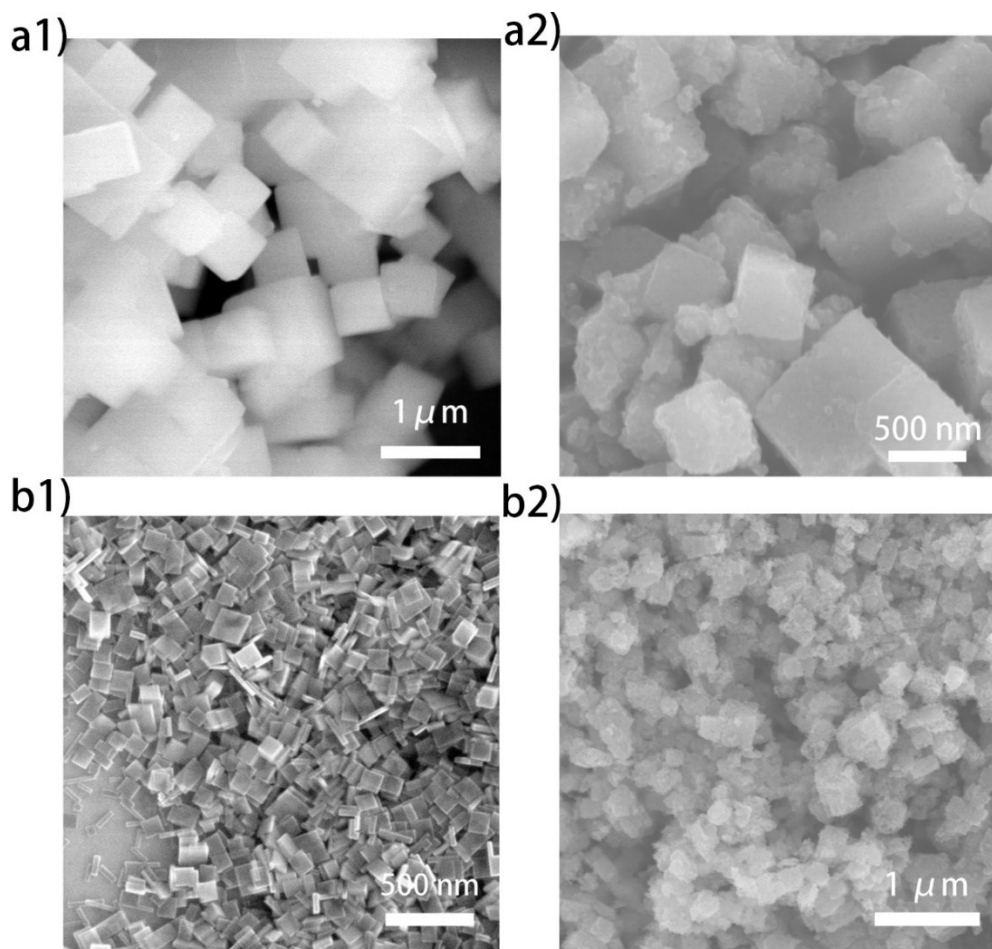
Figure S11. CV curves of $Co_{0.6}Fe_{0.4}P$-1.125 in the potential range of 0.72 to 1.42 V for calculating the effective fraction of active $Co_{0.6}Fe_{0.4}P$ sites, showing its irreversible electrochemical oxidation in 1.0 M KOH
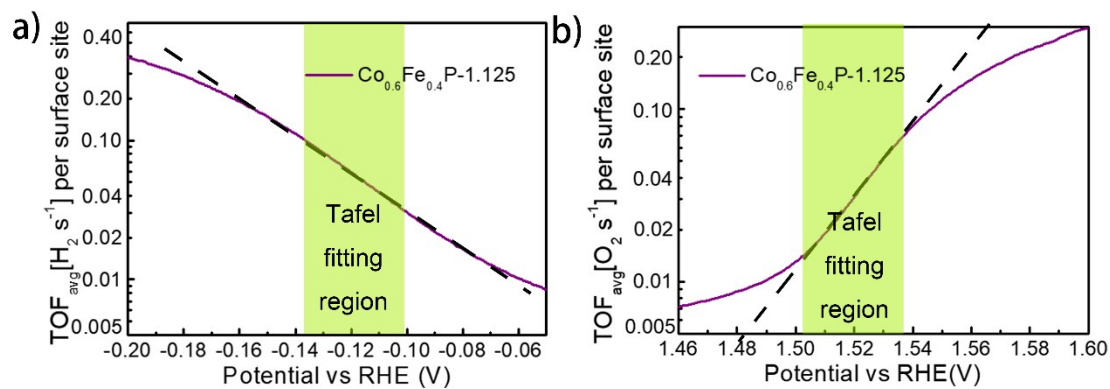
Figure S12. a) TOF curves of $Co_{0.6}Fe_{0.4}P$-1.125 for HER; b) TOF curves of $Co_{0.6}Fe_{0.4}P$-1.125 for OER.

Figure S13. SEM images of the as prepared a1) Co-Co PBA, b1) Fe-Fe PBA, and phosphorized a2) CoP, b2) FeP.
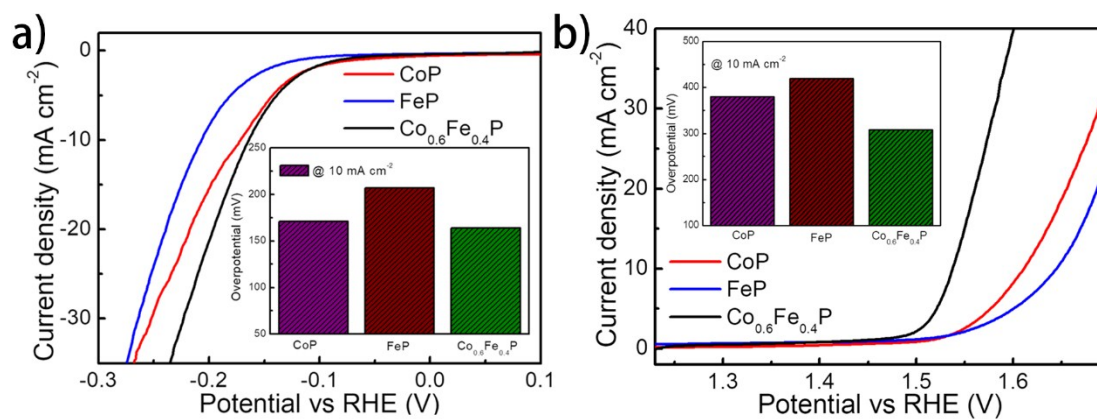
Figure S14. a) HER and b) OER activities of the as-prepared CoP and FeP vs. the bimetallic $Co_{0.6}Fe_{0.4}P$.
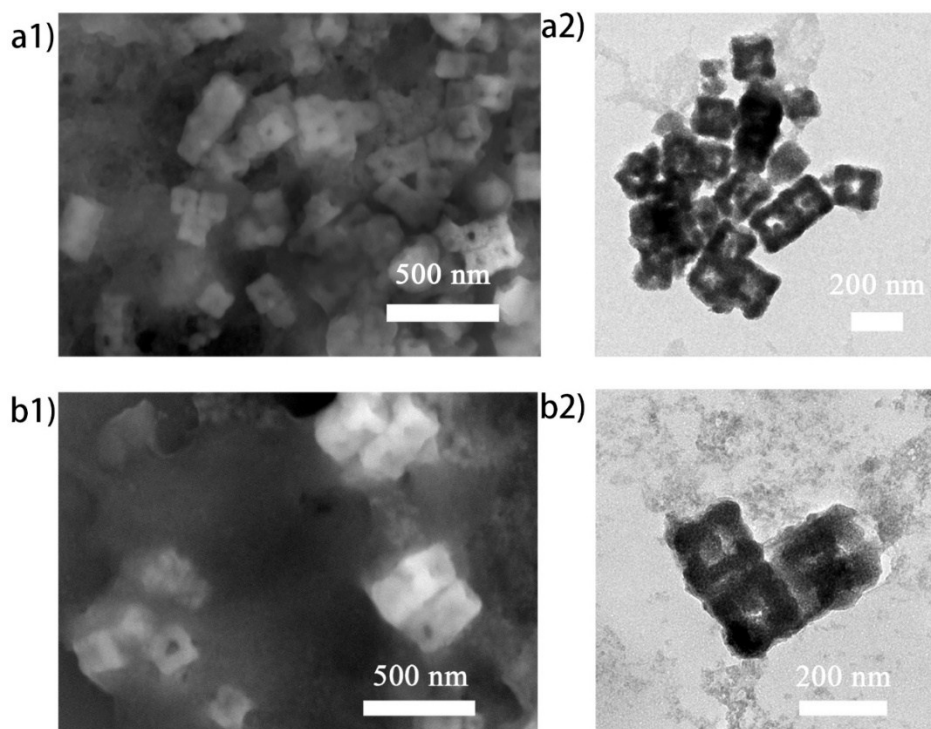
Figure S15. a1) SEM and a2) TEM images of the post-HER $Co_{0.6}Fe_{0.4}P$-1.125 sample; b1) SEM and b2) TEM images of the post-OER $Co_{0.6}Fe_{0.4}P$-1.125 sample. Residues of Nafion are visible in all images.

|	C (At%)	N (At%)	O (At%)	P (At%)	Fe (At%)	Co (At%)
CoFeP NF	22.66	2.92	17.71	32.12	9.49	12.41
Post-HER	26.77	4.99	34.76	15.81	6.91	10.77
Post-OER	28.29	4.04	45.78	1.37	8.27	12.26
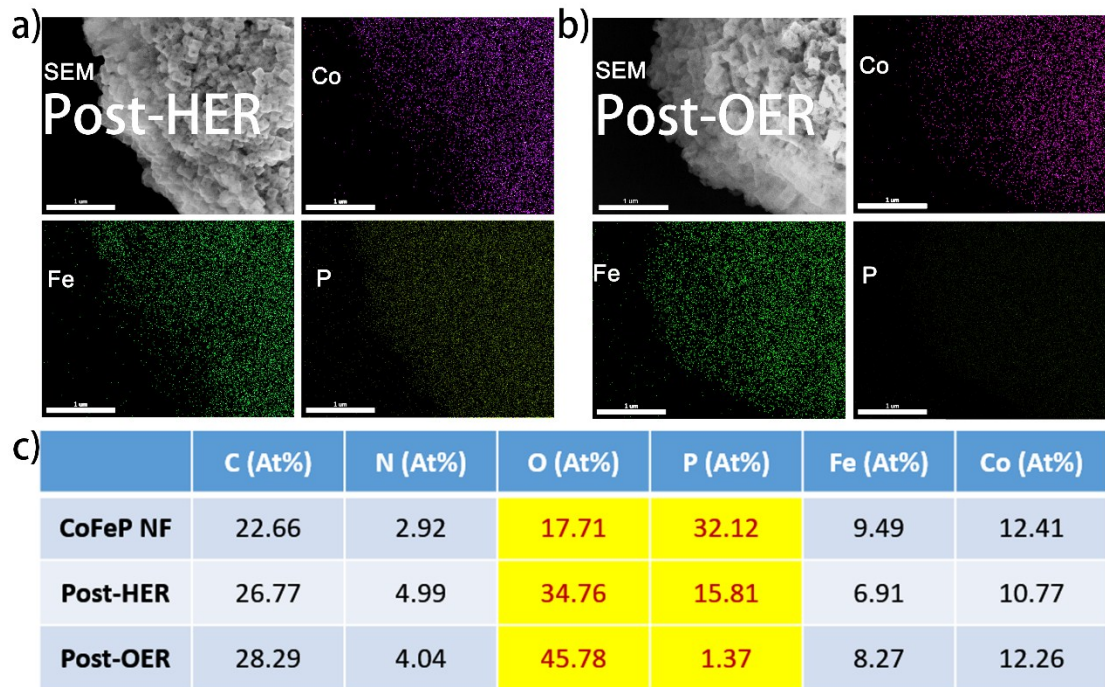
Figure S16. a) EDX mapping of the Co, Fe, P elements for the post-HER $Co_{0.6}Fe_{0.4}P$-1.125 sample; b) EDX mapping of the Co, Fe, P elements for the post-OER $Co_{0.6}Fe_{0.4}P$-1.125 sample; c) The element content of the as-prepared $Co_{0.6}Fe_{0.4}P$-1.125, post-HER $Co_{0.6}Fe_{0.4}P$-1.125 and post-OER $Co_{0.6}Fe_{0.4}P$-1.125 quantified by EDX.
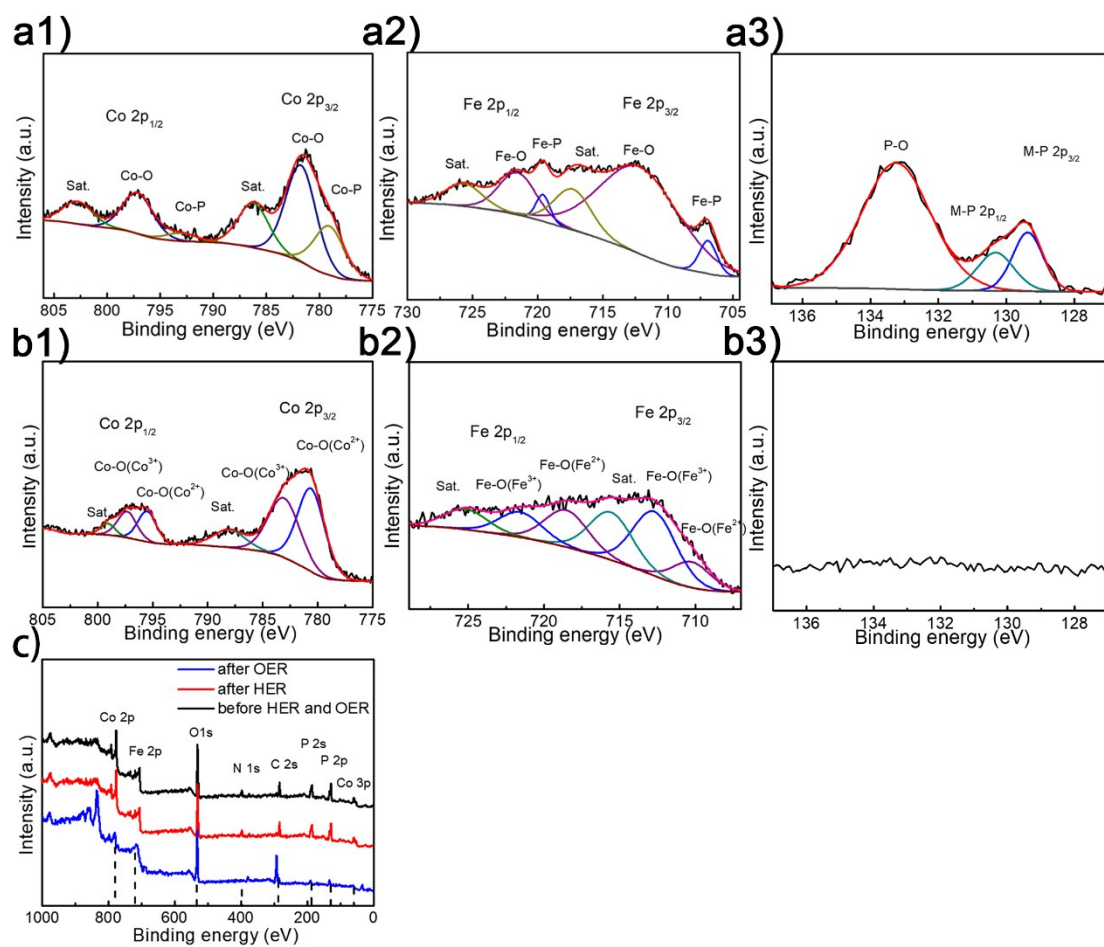
**Figure S17.** High-resolution XPS spectra of post-HER and post-OER $Co_{0.6}Fe_{0.4}P$-1.125 samples. a1) Co 2p, a2) Fe 2p, a3) P 2p spectra of the post-HER $Co_{0.6}Fe_{0.4}P$-1.125; b1) Co 2p, b2) Fe 2p, b3) P 2p spectra of the post-OER $Co_{0.6}Fe_{0.4}P$-1.125; c) XPS survey spectrum of the as-prepared $Co_{0.6}Fe_{0.4}P$-1.125, post-HER $Co_{0.6}Fe_{0.4}P$-1.125 and post-OER $Co_{0.6}Fe_{0.4}P$-1.125.
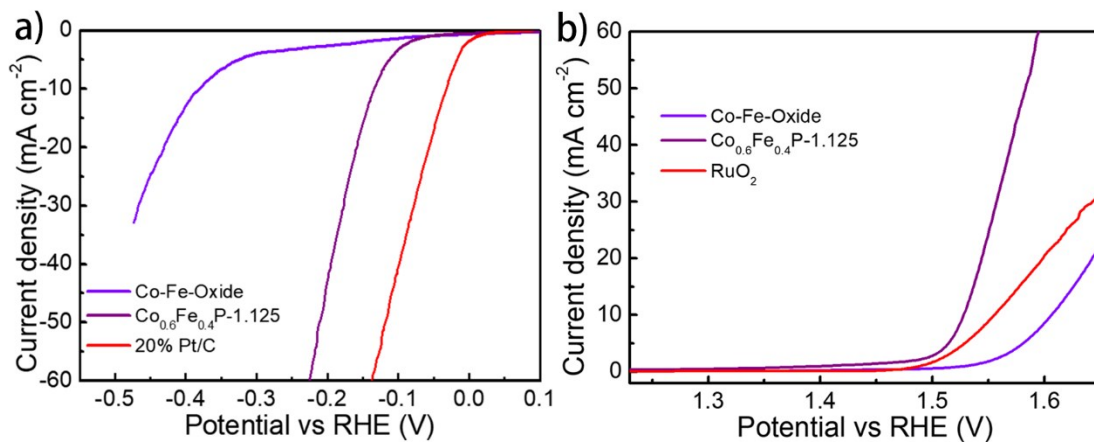
Figure S18. a) HER LSV curves of the Co-Fe oxide in 1.0 M KOH; b) OER LSV curves of the Co-Fe oxide in 1.0 M KOH.
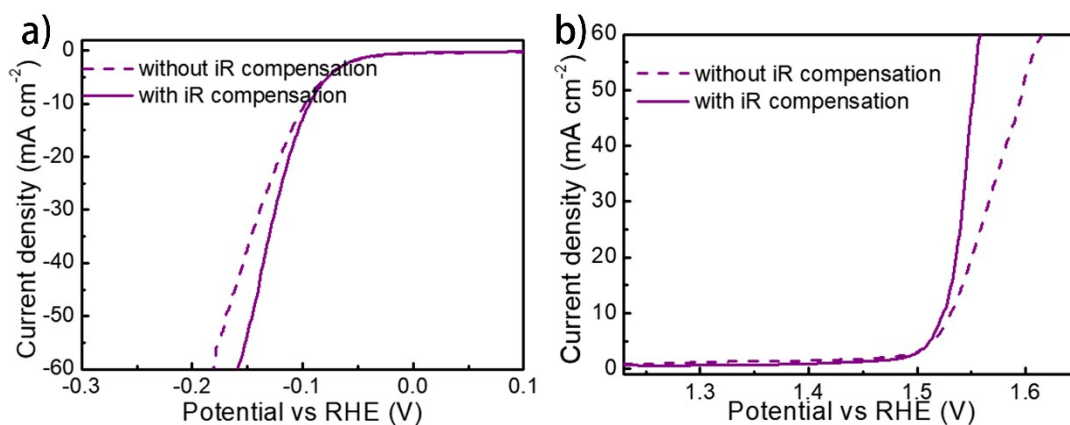
Figure S19. a) HER LSV curves of the $Co_{0.6}Fe_{0.4}P$-1.125 catalyst in 0.5 M H_2SO_4 with and without iR correction; b) OER LSV curves of the $Co_{0.6}Fe_{0.4}P$-1.125 catalyst in 1.0 M KOH with and without iR correction.
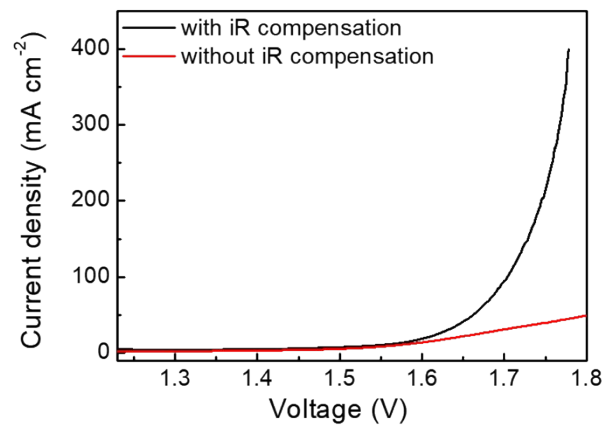
Figure S20. a) Overall water splitting LSV curves of the $Co_{0.6}Fe_{0.4}P$-1.125 catalyst coated on NF with and without iR correction.
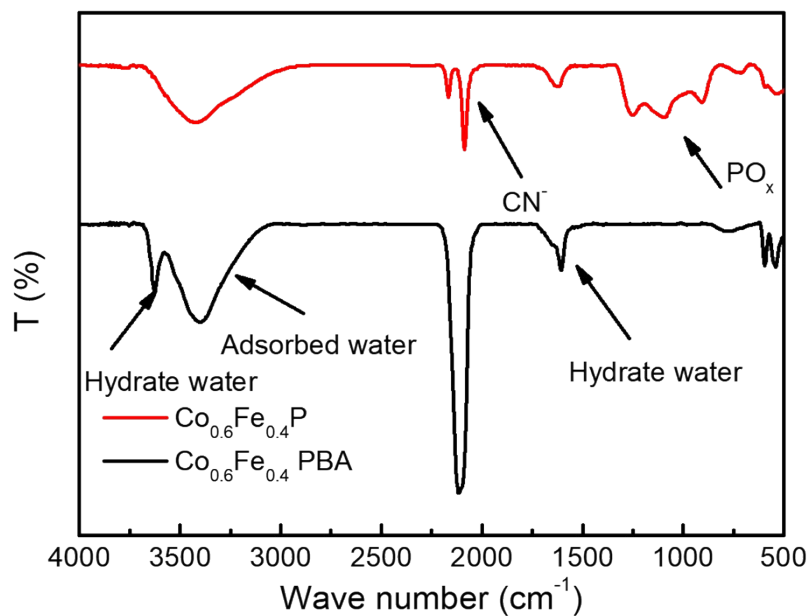
Figure S21. FTIR spectra of the as-prepared $Co_{0.6}Fe_{0.4}$-1.125 PBA and $Co_{0.6}Fe_{0.4}P$-1.125.
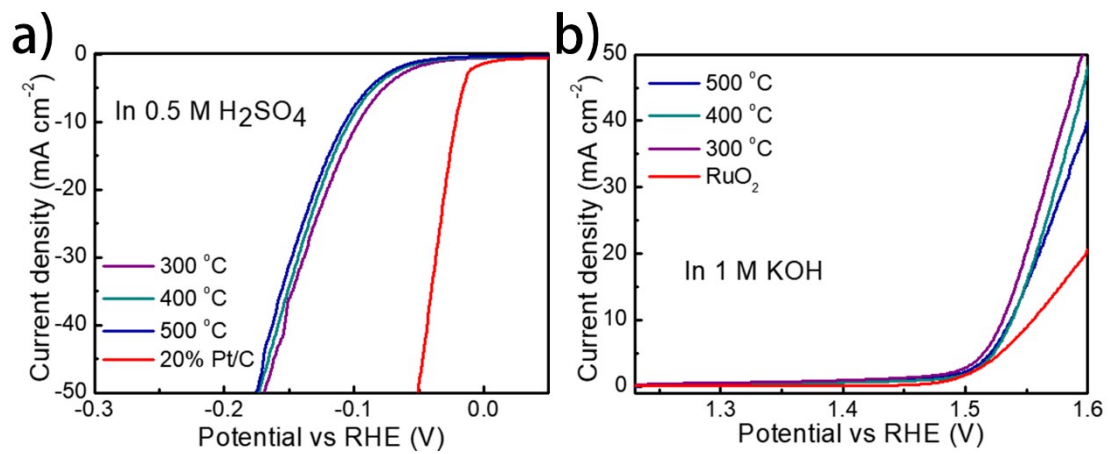
Figure S22. a) HER and b) OER activities of the bimetallic $Co_{0.6}Fe_{0.4}P$-1.125 phosphorized at different temperature.

Table S2. Summary of recent reports in high-performance bifunctional catalytic electrodes for overall water splitting.

Catalysts	Cell Voltages /V	Electrolyte	Reference
$Co_{0.6}Fe_{0.4}P$	10 mA cm^{-2} @ 1.58 V	1.0 M KOH	This work
NC@CuCo$_2$Nx/CF	10 mA cm^{-2} @ 1.62 V	1.0 M KOH	[1]
Ni$_3$S$_2$/NF	~13 mA cm^{-2} @ ~1.76 V	1.0 M KOH	[2]
NiS/Ni$_2$P/CC	10 mA cm^{-2} @ ~1.62 V	1.0 M KOH	[3]
Ni$_2$P/NF	10 mA cm^{-2} @ 1.57 V	1.0 M KOH	[4]
Co$_9$S$_8$/WS$_2$	<10 mA cm^{-2} @ 1.65 V	1.0 M KOH	[5]
Ni$_{0.69}$Co$_{0.31}$P	10 mA cm^{-2} @1.59 V	1.0 M KOH	[6]
NiCo$_2$O$_4$	10 mA cm^{-2} @1.65 V	1.0 M KOH	[7]
NiCoP/Ti	10 mA cm^{-2} @1.64 V	1.0 M KOH	[8]
Co$_3$S$_4$@MoS$_2$	10 mA cm^{-2} @ 1.58 V	1.0 M KOH	[9]
Co$_4$Ni$_1$P /NF	10 mA cm^{-2} @ 1.59 V	1.0 M KOH	[10]
porous MoO$_2$/NF	10 mA cm^{-2} @ 1.53 V	1.0 M KOH	[11]
Ni$_3$ZnC$_{0.7}$-550/NF	10 mA cm^{-2} @1.65 V	1.0 M KOH	[12]
Ni@NC-800/NF	10 mA cm^{-2} @1.60 V	1.0 M KOH	[13]
Ni–P foam	10 mA cm^{-2} @1.64 V	1.0 M KOH	[13]
MoS$_2$/Ni$_3$S$_2$	10 mA cm^{-2} @ 1.56 V	1.0 M KOH	[14]
NC-800/NF	18 mA cm^{-2} @ 1.62 V	1.0 M KOH	[15]
Cu@NiFe LDH	10 mA cm^{-2} @ 1.54 V	1.0 M KOH	[16]
Co-P	10 mA cm^{-2} @1.65 V	1.0 M KOH	[17]
NixCo$_3$–xS4/Ni$_3$S$_2$/NF	10 mA cm^{-2} @ 1.53 V	1.0 M KOH	[18]
Ni–Co–P hollow nanobricks	10 mA cm^{-2} @1.62 V	1.0 M KOH	[19]
Ni-Fe-P Porous Nanorods	10 mA cm^{-2} @1.52V	1.0 M KOH	[20]
Fe- and O-doped Co$_2$P /NF	10 mA cm^{-2} @1.56 V	1.0 M KOH	[21]
NiCo$_2$O$_4$	10 mA cm^{-2} @1.65 V	1.0 M KOH	[22]
FeP/Ni$_2$P	10 mA cm^{-2} @1.65 V	1.0 M KOH	[23]

Reference

[1]   J. Zheng, X. L. Chen, X. Zhong, S. Q. Li, T. Z. Liu, G. L. Zhuang, X. N. Li, S. W. Deng, D. H. Mei, J. G. Wang, *Advanced Functional Materials* **2017**, 27, 1704169.

[2]   L. L. Feng, G. T. Yu, Y. Y. Wu, G. D. Li, H. Li, Y. H. Sun, T. Asefa, W. Chen, X. X. Zou, *Journal of the American Chemical Society* **2015**, 137, 14023.

[3]   Q. Li, D. W. Wang, C. Han, X. Ma, Q. Q. Lu, Z. C. Xing, X. R. Yang, *Journal of Materials Chemistry A* **2018**, 6, 8233.

[4]   J. Y. Li, J. Li, X. M. Zhou, Z. M. Xia, W. Gao, Y. Y. Ma, Y. Q. Qu, *Acs Applied Materials & Interfaces* **2016**, 8, 10826.

[5]   S. J. Peng, L. L. Li, J. Zhang, T. L. Tan, T. R. Zhang, D. X. Ji, X. P. Han, F. Y. Cheng, S. Ramakrishna, *Journal of Materials Chemistry A* **2017**, 5, 23361.

[6]   Z. X. Yin, C. L. Zhu, C. Y. Li, S. Zhang, X. T. Zhang, Y. J. Chen, *Nanoscale* **2016**, 8, 19129.

[7]   M. Ledendecker, C. S. Krick, C. Papp, H. P. Steinrück, M. Antonietti, M. Shalom, *Angewandte Chemie International Edition* **2015**, 54, 12361.

[8]   C. Z. Yuan, S. L. Zhong, Y. F. Jiang, Z. K. Yang, Z. W. Zhao, S. J. Zhao, N. Jiang, A. W. Xu, *Journal of Materials Chemistry A* **2017**, 5, 10561.

[9]   Y. N. Guo, J. Tang, Z. L. Wang, Y. M. Kang, Y. Bando, Y. Yamauchi, *Nano Energy* **2018**, 47, 494.

[10]   L. Yan, L. Cao, P. Dai, X. Gu, D. Liu, L. Li, Y. Wang, X. Zhao, *Advanced Functional Materials* **2017**, 27, 1703455.

[11]   Y. S. Jin, H. T. Wang, J. J. Li, X. Yue, Y. J. Han, P. K. Shen, Y. Cui, *Advanced Materials* **2016**, 28, 3785.

[12]   J. Tian, Q. Liu, A. M. Asiri, X. Sun, *Journal of the American Chemical Society* **2014**, 136, 7587.

[13]   X. G. Wang, W. Li, D. H. Xiong, L. F. Liu, *Journal of Materials Chemistry A* **2016**, 4, 5639.

[14]   J. Zhang, T. Wang, D. Pohl, B. Rellinghaus, R. Dong, S. Liu, X. Zhuang, X. Feng, *Angewandte Chemie International Edition* **2016**, 55, 6702.

[15]   Y. Xu, W. Tu, B. Zhang, S. Yin, Y. Huang, M. Kraft, R. Xu, *Advanced Materials* **2017**, 29, 1605957.

[16]   L. Yu, H. Q. Zhou, J. Y. Sun, F. Qin, F. Yu, J. M. Bao, Y. Yu, S. Chen, Z. F. Ren, *Energy & Environmental Science* **2017**, 10, 1820.

[17] H. F. Liang, A. N. Gandi, D. H. Anjum, X. B. Wang, U. Schwingenschlogl, H. N. Alshareef, *Nano Letters* **2016**, 16, 7718.

[18] Y. Wu, Y. Liu, G. D. Li, X. Zou, X. Lian, D. Wang, L. Sun, T. Asefa, X. Zou, *Nano Energy* **2017,** 35, 161.

[19] E. L. Hu, Y. F. Feng, J. W. Nai, D. Zhao, Y. Hu, X. W. Lou, *Energy & Environmental Science* **2018**, 11, 872.

[20] S. H. Ahn, A. Manthiram, *Journal of Materials Chemistry A* **2017**, 5, 2496.

[21] J. Duan, S. Chen, A. Vasileff, S. Z. Qiao, *ACS Nano* **2016**, 10, 8738.

[22] X. Gao, H. Zhang, Q. Li, X. Yu, Z. Hong, X. Zhang, C. Liang, Z. Lin, *Angewandte Chemie International Edition* **2016**, 55, 6290.

[23] F. Yu, H. Zhou, Y. Huang, J. Sun, F. Qin, J. Bao, W. A. Goddard, S. Chen, Z. Ren, *Nature Communications* DOI:10.1038/s41467-018-04746-z